



## Enhancing tungsten oxide/SBA-15 catalysts for hydrolysis of cellobiose through doping ZrO<sub>2</sub>



Hua Wang<sup>a</sup>, Yingge Guo<sup>a</sup>, Cuirong Chang<sup>a</sup>, Xinli Zhu<sup>a,\*</sup>, Xiao Liu<sup>a</sup>, Jinyu Han<sup>a</sup>, Qingfeng Ge<sup>a,b,\*\*</sup>

<sup>a</sup> Key Laboratory for Green Chemical Technology, School of Chemical Engineering and Technology, Tianjin University; Collaborative Innovation Center of Chemical Science and Engineering, Tianjin 300072, China

<sup>b</sup> Department of Chemistry and Biochemistry, Southern Illinois University, Carbondale, IL 62901, USA

### ARTICLE INFO

#### Article history:

Received 10 April 2016

Received in revised form 30 May 2016

Accepted 4 June 2016

#### Keywords:

Cellobiose

Hydrolysis

Glucose

WZr/SBA-15

Biomass conversion

### ABSTRACT

The number of strong acid sites on a hydrolysis catalyst accessible by the bulky cellulose limits its efficiency in the conversion and utilization of biomass-based resources. In this work, high surface area WZr/SBA-15 catalysts ( $>400\text{ m}^2/\text{g}$ ) were prepared by hydrothermal method and characterized using XRD, N<sub>2</sub> adsorption, TEM, Raman, UV-vis, XPS and FTIR of pyridine adsorption. The results showed that doping a moderate amount of ZrO<sub>2</sub> into the WO<sub>3</sub>/SBA-15 catalyst stabilized the tungstate species in the form of a polytungstate species as a result of the strong ZrO<sub>x</sub>-WO<sub>x</sub> interaction as well as increased the surface area of the catalyst. The resulting polytungstate species provided strong Brønsted acid sites for hydrolysis. Consequently, the cellobiose conversion was maximized at 5% ZrO<sub>2</sub> loading, corresponding to a maximized surface area and density of Brønsted acid sites. This catalytic activity is significantly higher than that of a WO<sub>3</sub>/ZrO<sub>2</sub> catalyst prepared using the conventional impregnation method, indicating the importance of mesoporous structure to the dispersion of active species and to the accessibility of the active sites by the bulky reactant. This result indicates that the density of the strong Brønsted acid sites with improved accessibility by the bulky reactant is essential to achieve a high hydrolysis activity.

© 2016 Elsevier B.V. All rights reserved.

### 1. Introduction

Production of fuels and chemicals from renewable biomass resources is important to a sustainable development of our society [1,2]. Cellulose exists widely in biomass resources [3,4], can be converted to various value-added platform molecules as well as biofuels through different chemical transformations [5–9]. However, chemical conversion of cellulose is challenging due to the strong intermolecular and intramolecular hydrogen bonds between glycosidic units. The first step in the conversion of cellulose is to depolymerize the polysaccharide through hydrolysis into soluble oligosaccharides and glucose, a versatile precursor to produce valuable chemicals such as biodegradable plastics and ethanol [10–12]. Conventional hydrolysis process uses inorganic liquid acid (such as H<sub>2</sub>SO<sub>4</sub> and HCl) as catalyst, which burdens the

post-processing and recycling. Therefore, considerable efforts have been devoted to develop various solid acid catalysts for hydrolysis of cellulose [13–15].

Only a few solid acid catalysts can attain a high yield of sugars for hydrolyzing cellulose without pretreatments such as ball-milling, acid or alkali treatments [16–20]. It is generally accepted that the strong Brønsted acid sites are responsible for hydrolyzing the  $\beta$ -1,4-glycosidic bonds of cellulose. WO<sub>3</sub>/ZrO<sub>2</sub>, known as a super strong solid acid, contains both strong Brønsted and Lewis acid sites and has been explored in the hydrolysis of cellulose. Kourieh [21] reported a conversion of 12% at 97 °C for hydrolysis of cellobiose on the co-precipitated WO<sub>3</sub>/ZrO<sub>2</sub> catalysts with a surface area of 100  $\text{m}^2/\text{g}$  with reaction time of 30 h. More recently, Chambon et al. [22] studied hydrolysis of cellulose on an anionic exchanged WO<sub>3</sub>/ZrO<sub>2</sub> catalyst with a surface area of 218  $\text{m}^2/\text{g}$ . These authors found the major product was lactic acid at 190 °C and in 5 MPa He and a high yield of lactic acid would require a long reaction time of 30 h. The relative low conversion may be a result of the low surface area of WO<sub>3</sub>/ZrO<sub>2</sub>, which limited the number of acid sites accessible to the bulky reactants of cellulose and its derivatives.

WO<sub>3</sub>/ZrO<sub>2</sub> has been widely used in acid-catalyzed reactions, such as dehydration and cracking [23–29]. A number of attempts

\* Corresponding author at: School of Chemical Engineering and Technology, Tianjin University, Tianjin 300072, China.

\*\* Corresponding author at: Department of Chemistry and Biochemistry, Southern Illinois University, Carbondale, IL 62901, USA.

E-mail addresses: [xinlizhu@tju.edu.cn](mailto:xinlizhu@tju.edu.cn) (X. Zhu), [qge@chem.siu.edu](mailto:qge@chem.siu.edu) (Q. Ge).

have been made to obtain high surface area W/Zr catalysts through various preparation methods. Cheng et al. [30] introduced a mixture of W/Zr oxides on various porous silica materials by co-impregnation and applied these catalysts in *n*-pentane isomerization. Jiménez-López et al. [31] prepared a series of catalysts by supporting  $\text{WO}_3$  on Zr-doped MCM-41 using impregnation and used the catalysts for the esterification of oleic acid with methanol. Recently, Yi and co-workers [32] synthesized Zr- $\text{WO}_x$  modified mesoporous  $\text{SiO}_2$  catalysts using a refined hydrothermal method for esterification of 1-butanol with acetic acid, which exhibited much higher activity than HZSM-5 and conventional  $\text{WO}_3/\text{ZrO}_2$  catalysts.

In this work, high surface area WZr/SBA-15 catalysts were prepared by hydrothermal method and characterized using a variety of techniques to understand its nature and structure. The correlation of the structure of the catalysts with their catalytic performance for the hydrolysis of cellobiose was investigated. We found that doping proper amount of  $\text{ZrO}_2$  in W/SBA-15 maximized its surface area and accessible strong acid sites, both contributed to a remarkably increased activity for the hydrolysis of cellobiose to glucose and mannose.

## 2. Experimental

### 2.1. Catalyst preparation

#### 2.1.1. Chemicals

Hydrochloric acid (37%) and ethanol were purchased from Tianjin Kermel Chemical Reagent. Pluronic P123 was obtained from Sigma-Aldrich. Zirconium butoxide solution (80 wt.% in *n*-butanol) and ammonium metatungstate ( $(\text{NH}_4)_6\text{H}_2\text{W}_{12}\text{O}_{40} \cdot x\text{H}_2\text{O}$ ) were purchased from Tianjin Heowns Bio-Chem Technology. Zirconyl chloride octahydrate ( $\text{ZrOCl}_2 \cdot 8\text{H}_2\text{O}$ ), sodium tungstate dihydrate ( $\text{Na}_2\text{WO}_4 \cdot 2\text{H}_2\text{O}$ ) and tetraethyl orthosilicate (TEOS) were obtained from Aladdin.

#### 2.1.2. Synthesis of the mesoporous WZr/SBA-15

The synthesis of the mesoporous WZr/SBA-15 followed the procedure reported by Yi [32]. Typically, pluronic 123 (2 g) was dissolved in a mixture of de-ionized water (60 mL) and concentrated hydrochloric acid (6 mL). The mixture was stirred for 4 h until a clear solution was obtained. Zirconium butoxide ethanol solution (v/v = 1) was added drop-wise to the solution under vigorous stirring. Then, an aqueous solution of sodium tungstate (3 mL) was added drop-wise and stirred for another 1 h. TEOS of 4.17 g was introduced to the solution, which was then stirred at 40 °C for 24 h. Hydrothermal synthesis was carried out at 100 °C for 24 h. The resulting precipitate was filtered and washed with ethanol and de-ionized water several times. Finally, it was dried at 80 °C overnight and calcined at 550 °C for 3 h. The catalysts are denoted as  $\text{W}_x\text{Zr}_y/\text{SBA}-15$ , with  $x$  and  $y$  being the  $\text{WO}_3$  and  $\text{ZrO}_2$  weight percentage of the catalyst, respectively.

#### 2.1.3. Synthesis of $\text{ZrO}_2/\text{SBA}-15$ and $\text{WO}_3/\text{SBA}-15$

7.1%  $\text{ZrO}_2/\text{SBA}-15$  and 31.6%  $\text{WO}_3/\text{SBA}-15$  were prepared using the same procedure as the WZr/SBA-15 catalysts without the addition of sodium tungstate or zirconium butoxide, respectively.

#### 2.1.4. Synthesis of $\text{WO}_3/\text{ZrO}_2$

$\text{WO}_3/\text{ZrO}_2$  was prepared using a conventional impregnation method [27]. Briefly, concentrated ammonia was added slowly to an aqueous solution of zirconyl chloride octahydrate until pH = 10. After stirring and aging, the precipitate was separated by centrifugation and then dried. The as-prepared precipitate was impregnated with an aqueous solution of ammonium metatungstate, followed by calcination at 550 °C (for 30%

$\text{WO}_3/\text{ZrO}_2$ , which was used for comparison with WZr/SBA-15 samples prepared at the same calcination temperature and with same amount of  $\text{WO}_3$  loadings) and 700 °C (for 20%  $\text{WO}_3/\text{ZrO}_2$ , which was the optimized condition to achieve the highest amounts of Zr-WO<sub>3</sub> in the  $\text{WO}_3/\text{ZrO}_2$  catalysts in reference [27]) for 3 h, respectively. A reference  $\text{WO}_3$  rich catalyst (denoted as  $\text{W}_{30}\text{Zr}_5$ ) with  $\text{WO}_3:\text{ZrO}_2$  ratio of 30:5 was prepared using the same method described above, followed calcination at 550 °C for 3 h.

## 2.2. Characterizations

The nitrogen adsorption-desorption isotherms were obtained on a Tristar 3000 (Micrometrics). Prior to measurements, samples were outgassed at 90 °C for 1 h and then at 300 °C for 3 h. The specific surface area was calculated using the BET method. The mesopore size distribution was obtained by applying the BJH method to the adsorption branch of the isotherm.

Powder X-ray diffraction (XRD) was performed on a D/MAX-2500 (Rigaku Corporation, Japan) XD-3A diffractometer using a Cu K $\alpha$  radiation source, operated at 40 kV and 100 mA. The XRD patterns were measured in the  $2\theta$  range of 0.5–5° and 10–90° at a scanning speed of 0.5°/min and 4°/min, respectively.

Transmission electron microscopy (TEM) images were obtained on a JEM-1400 microscope (JOEL). Samples of fine powder were suspended in ethanol with an ultrasonic treatment for 30 min and then deposited on carbon-coated copper grids for TEM observations.

Raman spectroscopy was recorded on a DXR Microscope. The He-Cd laser of 532 nm was employed as the exciting source with an incident power of 30 mW.

Diffuse-reflectance ultraviolet-visible spectroscopy (DR UV-vis) spectra were acquired using a UV-2550 spectrophotometer (Shimadzu Corporation, Japan).

X-ray photoelectron spectra (XPS) were measured on a PHI 1600 (PerkinElmer). All binding energies were calibrated using the C<sub>1s</sub> peak at 284.8 eV as the reference.

The pyridine adsorption FTIR spectra were recorded by a MAGNA-IR 560 spectrometer. In each measurement, self-supporting wafer (50 mg, 13 mm diameter) was first evacuated in situ at 400 °C for 1 h, followed by adsorption of pyridine at 60 °C for 30 min. The spectra were recorded at 150 °C after desorption. The acid densities of Brønsted acid site and Lewis acid site were estimated using the following equations [33]:

$$C_B = 1.88IA_BR^2/W \quad (1)$$

$$C_L = 1.42IA_LR^2/W \quad (2)$$

where,  $C_B$  is the density of Brønsted acid site (mmol/g<sub>cat</sub>),  $C_L$  is the density of Lewis acid site (mmol/g<sub>cat</sub>),  $IA_B$  and  $IA_L$  are the integrated absorbance of Brønsted and Lewis band (cm<sup>-1</sup>), respectively,  $R$  is the radius of disk (0.65 cm),  $W$  is the weight of disk (mg). 1.88 and 1.42 are the molar extinction coefficients ( $\mu\text{mol}/\text{cm}$ ) of pyridine adsorption on Brønsted acid site and Lewis acid site, respectively.

The acidic properties of the samples were also characterized by temperature programmed desorption of ammonia (NH<sub>3</sub>-TPD) in a micro reactor equipped with a Cirrus 200 mass spectrometer (MKS), as reported in previous work [34,35]. Catalyst sample of 50 mg was pretreated for 1 h in flowing He (30 mL/min) at 350 °C to eliminate any adsorbed water. After it was cooled down to 50 °C, the sample was exposed to 5% NH<sub>3</sub>/He (30 mL/min) for 30 min, followed by flushing with He (30 mL/min) for another 30 min to remove the physically adsorbed NH<sub>3</sub>. Then the sample was heated to 800 °C at a heating rate of 10 °C/min.

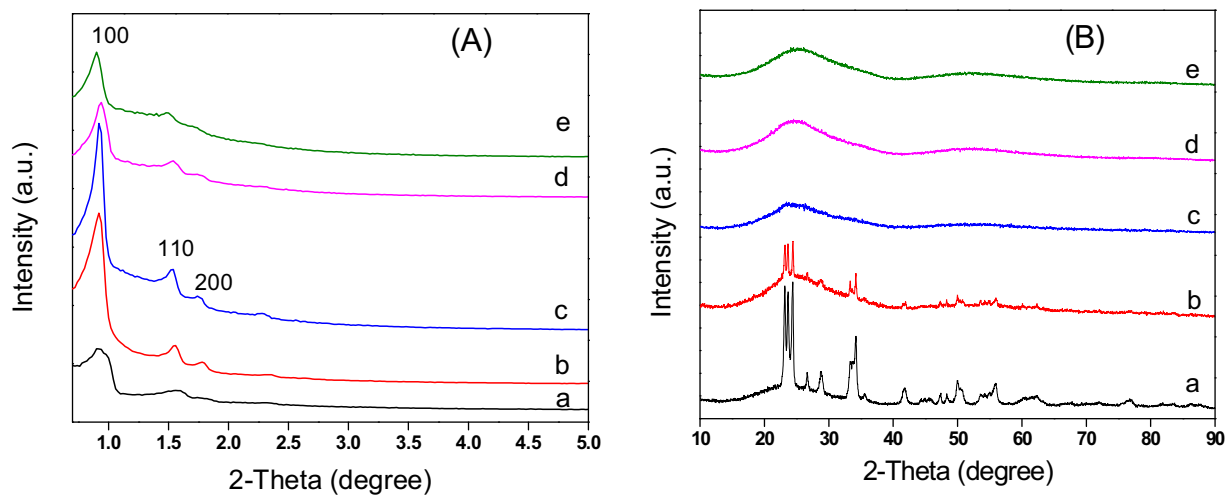


**Fig. 1.** XRD patterns of (a)  $\text{W}_{30}\text{Zr}_0/\text{SBA-15}$ , (b)  $\text{W}_{30}\text{Zr}_3/\text{SBA-15}$ , (c)  $\text{W}_{30}\text{Zr}_5/\text{SBA-15}$ , (d)  $\text{W}_{30}\text{Zr}_{10}/\text{SBA-15}$ , (e)  $\text{W}_{30}\text{Zr}_{15}/\text{SBA-15}$  in (A) small-angle region and (B) wide-angle region.

### 3.2. Catalytic reaction

Cellobiose hydrolysis was carried out in a steel autoclave with a Teflon liner (50 mL), equipped with a magnetic stirrer. Typically, 0.20 g cellobiose, 0.1 g catalyst, and 20 mL  $\text{H}_2\text{O}$  were added. Then, the system was sealed and flushed with nitrogen for several times and finally pressurized to 2.5 MPa in nitrogen. The reactions were carried out at 160 °C for 90 min with magnetic stirring at 600 r/min. After reaction, the solid catalyst was separated by centrifugation. The liquid phase was analyzed by high performance liquid chromatography (HPLC) equipped with an ICsep ICE-Coregel 87H3 column and a RID detector. The HPLC column was retained at 38 °C, using  $\text{H}_2\text{SO}_4$  solution (5 mM, 0.6 mL/min) as the mobile phase. The yields were calculated as the molar ratio of the product and the initial cellobiose, corrected by the number of carbon atoms[20]. The products were qualified by injection of standard samples and quantified by application of calibration curves prepared by using external standards (See the detail in the supporting information).

## 4. Results and discussion

### 4.1. Structural characterization (XRD, BET and TEM)

Fig. 1 shows the XRD patterns of the  $\text{W}_{30}\text{Zr}_y/\text{SBA-15}$  catalysts with varying  $\text{ZrO}_2$  content (0–15%). In small-angle region (Fig. 1A), all samples exhibit three peaks at 0.5–2° that can be indexed to  $d_{100}$ ,  $d_{110}$  and  $d_{200}$  reflections of the 2D hexagonal mesoporous structures with  $p6mm$  symmetry, respectively. These results indicate that the SBA-15 structure was preserved even when a significant amount of  $\text{WO}_3$  and  $\text{ZrO}_2$  were loaded [36,37]. The  $d_{100}$  peak is

broad and the  $d_{110}$  and  $d_{200}$  peaks are hardly observable for the sample without  $\text{ZrO}_2$  (trace a), which suggests that 30%  $\text{WO}_3$  loading onto the SBA-15 leads to significant disruption to the structure, consistent with literature reports [38]. When the  $\text{ZrO}_2$  content is increased to 3 and 5% (trace b and c), the intensity of  $d_{100}$  increases markedly, with the  $d_{110}$  and  $d_{200}$  peaks being clearly observed. This indicates that adding small amount of zirconium has a positive effect on improving the ordered mesoporous structure. However, the intensities of  $d_{100}$ ,  $d_{110}$ , and  $d_{200}$  decrease as the  $\text{ZrO}_2$  content is further increased to 10 and 15% (trace d and e), indicating some degree of disorder of the mesopores when excessive amount of  $\text{ZrO}_2$  was doped.

In the wide-angle region (Fig. 1B), the  $\text{ZrO}_2$  free-sample (trace a) shows strong diffraction peaks at  $2\theta$  of 23.21, 23.61, 24.43, 26.61, 28.79, 34.26, 41.76, 50.08, and 55.96°, which can be assigned to monoclinic  $\text{WO}_3$  [38]. When 3%  $\text{ZrO}_2$  was doped, the intensity of diffraction peaks of monoclinic  $\text{WO}_3$  declined remarkably (trace b). The monoclinic  $\text{WO}_3$  diffraction peaks disappeared when the  $\text{ZrO}_2$  content exceeded 5% (trace c–e). Meanwhile, no diffraction peaks of  $\text{ZrO}_2$  can be observed, even when the  $\text{ZrO}_2$  content was increased up to 15%. These results indicate that the strong interaction between W and Zr species resulted in a highly dispersed  $\text{W}_{30}\text{Zr}_y\text{O}_z$  on SBA-15. It has been reported that the addition of a small amount of tungstate can stabilize zirconia through the strong interactions and prevent zirconia to transform from tetragonal to monoclinic crystallite [23,27]. In turn, the addition of the Zr species helps the dispersion of the W species, preventing the aggregation of the tungstate species into  $\text{WO}_3$  crystalline. Moreover, the Zr-stabilized  $\text{WO}_x$  nanoparticles may be in the form of amorphous particle or tiny crystalline and are highly dispersed on SBA-15.

**Table 1**

Textural property of mesoporous W $\text{Zr}/\text{SBA-15}$  materials.

Samples	$S_{\text{BET}}^{\text{a}}$ ( $\text{m}^2/\text{g}$ )	$V_{\text{total}}^{\text{b}}$ ( $\text{cm}^3/\text{g}$ )	BAS density <sup>c</sup> ( $\mu\text{mol/g}$ )	Total acid density <sup>c</sup> ( $\mu\text{mol/g}$ )	B/L <sup>d</sup>
$\text{W}_{30}\text{Zr}_0/\text{SBA-15}$	412	0.71	33.2	117.1	0.396
$\text{W}_{30}\text{Zr}_3/\text{SBA-15}$	457	0.82	58.6	172.0	0.516
$\text{W}_{30}\text{Zr}_5/\text{SBA-15}$	491	0.85	71.4	207.7	0.524
$\text{W}_{30}\text{Zr}_{10}/\text{SBA-15}$	461	0.81	64.3	193.4	0.497
$\text{W}_{30}\text{Zr}_{15}/\text{SBA-15}$	428	0.60	40.4	145.8	0.383

<sup>a</sup>  $S_{\text{BET}}$  is the surface area calculated by Brunauer–Emmett–Teller (BET) method.

<sup>b</sup> Total pore volume ( $V_p$ ) was calculated at  $P/P_0 = 0.97$ .

<sup>c</sup> Brønsted acid site (BAS) density and total acid density were measured by FT-IR spectra of pyridine adsorption.

<sup>d</sup> B/L is the ratio of BAS density and LAS density.

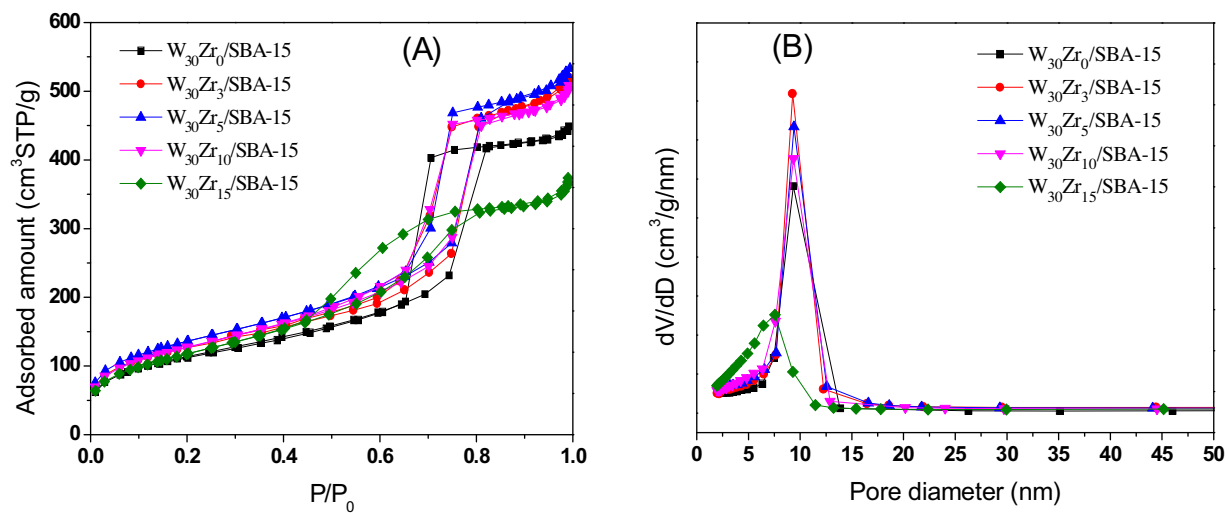


**Fig. 2.** N<sub>2</sub> adsorption-desorption isotherms (A) and pore size distribution (B) of mesoporous W<sub>30</sub>Zr<sub>y</sub>/SBA-15 ( $y = 0, 3, 5, 10, 15$ ) catalysts.

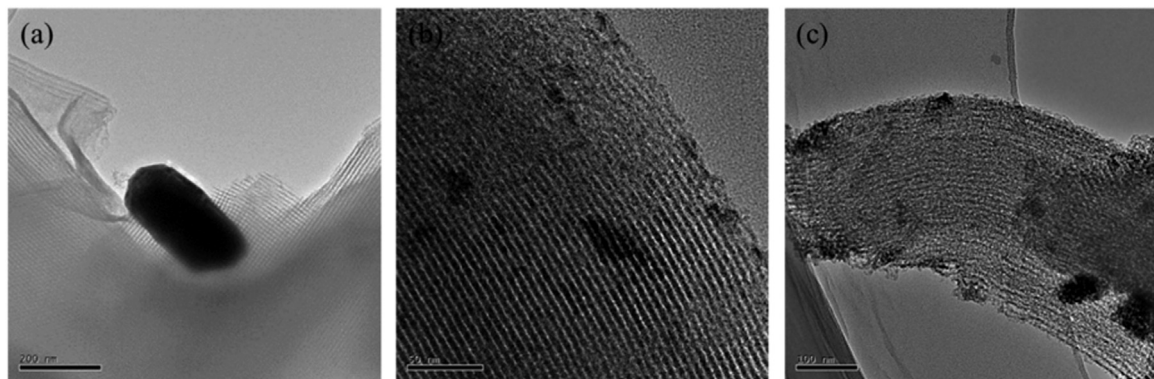


**Fig. 3.** TEM images of (a) W<sub>30</sub>Zr<sub>0</sub>/SBA-15, (b) W<sub>30</sub>Zr<sub>5</sub>/SBA-15, (c) W<sub>30</sub>Zr<sub>15</sub>/SBA-15.

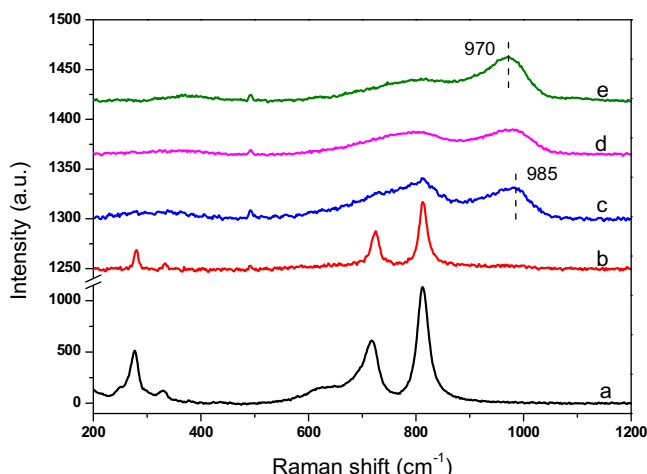
The N<sub>2</sub> adsorption–desorption isotherms and the BJH pore size distribution curves of the WZr/SBA-15 samples are depicted in Fig. 2. All samples exhibits the type IV isotherm with H1 hysteresis loop (Fig. 2A), indicating the preservation of mesoporous structure [36]. The hysteresis loops of W<sub>30</sub>Zr<sub>y</sub>/SBA-15 samples with the ZrO<sub>2</sub> content less than 10% are of similar shapes with clear capillary condensation at  $P/P_0 \sim 0.7$ , reflecting the presence of well-defined mesoporous channels with a narrow distribution of pore sizes [32]. As a result, the BJH derived pore size distribution centered at 9 nm is sharp and narrow for samples with ZrO<sub>2</sub> loading less than 10% (Fig. 2B). The shape of hysteresis loop is much different for W<sub>30</sub>Zr<sub>15</sub>/SBA-15, with significantly reduced adsorption at  $P/P_0 > \sim 0.7$  and the hysteresis extended to lower  $P/P_0$ . This may suggest that the morphology of the pore structure was changed when excess ZrO<sub>2</sub> was doped, perhaps due to pore narrowing and blockage as a result of the formation of larger aggregates of Zr-WO<sub>3</sub> at high ZrO<sub>2</sub> loadings. Consequently, the pore size of W<sub>30</sub>Zr<sub>15</sub>/SBA-15 was reduced to 7 nm, with non-uniform distributions. As summarized in Table 1, the specific surface area and total pore volume are maximized at the ZrO<sub>2</sub> loading of 5%, consistent with the XRD results. This result indicates that addition of appropriate amount of ZrO<sub>2</sub> could prevent aggregation of tungstate as well as stabilize the mesoporous structure of SBA-15.

Fig. 3 shows the representative TEM images of WZr/SBA-15 samples. All samples show the presence of the mesoporous structures. For W<sub>30</sub>Zr<sub>0</sub>/SBA-15, large WO<sub>3</sub> crystallites of 200 nm are observed on the external surface of SBA-15 (Fig. 3a). This is due to the weak

interaction of tungstate with silica, resulting in the migration of WO<sub>3</sub> out of the mesopores and aggregation on the external surface into large particles. For W<sub>30</sub>Zr<sub>5</sub>/SBA-15, only small particles inside the mesopores are observed (Fig. 3b), indicating that the addition of ZrO<sub>2</sub> with proper amount stabilizes WO<sub>3</sub> through a Si-Zr-W interaction and prevents aggregation of WO<sub>3</sub>. However, aggregates of <50 nm filling in the space between the mesopores are observed for W<sub>30</sub>Zr<sub>15</sub>/SBA-15 (Fig. 3c), suggesting that excessive ZrO<sub>2</sub> extracts WO<sub>3</sub> from the framework, which partly migrates to external surface due to the preferential interaction between the ZrO<sub>2</sub> and WO<sub>3</sub> species. Note that XRD did not show any diffraction feature of either ZrO<sub>2</sub> or WO<sub>3</sub> crystallites. Therefore, it is reasonable to assume that these aggregates are composed of Zr stabilized tiny WO<sub>3</sub> particles (Zr-WO<sub>3</sub>). These aggregates apparently would block the mesopores to some extent, resulting in lowered surface areas.

#### 4.2. Chemical environment of the W and Zr species (Raman, UV-vis and XPS)

The Raman spectra of WZr/SBA-15 catalysts are displayed in Fig. 4. W<sub>30</sub>Zr<sub>0</sub>/SBA-15 showed intense bands at 807, 720, and 273 cm<sup>-1</sup> (trace a), which can be assigned to W–O stretching, W–O bending and W–O–W deformation modes of monoclinic WO<sub>3</sub>, respectively [29,31,39]. For W<sub>30</sub>Zr<sub>3</sub>/SBA-15, the intensity of these bands decreased significantly (trace b). As the ZrO<sub>2</sub> content increased to 5%, the diffraction peaks of monoclinic WO<sub>3</sub> at 807, 720 cm<sup>-1</sup> turned into a broad peak at 750~850 cm<sup>-1</sup> (trace



**Fig. 4.** Raman spectra of (a)  $\text{W}_{30}\text{Zr}_0/\text{SBA-15}$ , (b)  $\text{W}_{30}\text{Zr}_3/\text{SBA-15}$ , (c)  $\text{W}_{30}\text{Zr}_5/\text{SBA-15}$ , (d)  $\text{W}_{30}\text{Zr}_{10}/\text{SBA-15}$ , (e)  $\text{W}_{30}\text{Zr}_{15}/\text{SBA-15}$ .

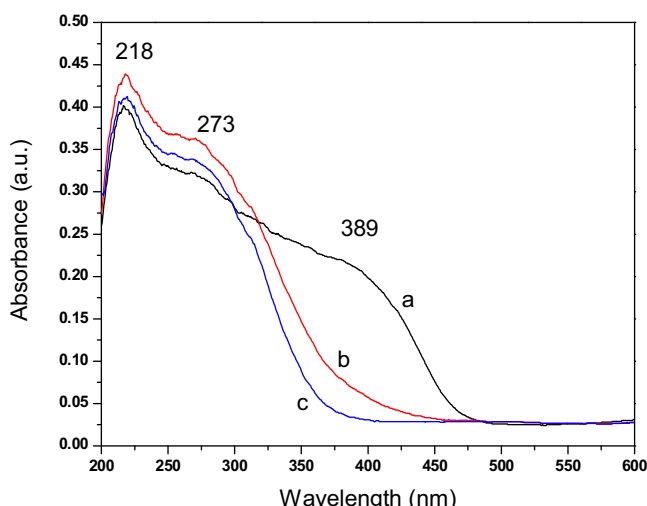


**Fig. 5.** Diffuse reflectance UV-vis spectra of (a)  $\text{W}_{30}\text{Zr}_0/\text{SBA-15}$ , (b)  $\text{W}_{30}\text{Zr}_5/\text{SBA-15}$ , (c)  $\text{W}_{30}\text{Zr}_{15}/\text{SBA-15}$  samples.

c), indicating a poor crystallinity of  $\text{WO}_3$  and the existence of tiny crystalline  $\text{WO}_3$  [27,40]. In addition, a new band centered at  $985 \text{ cm}^{-1}$  was observed, which is associated with the stretch mode of monooxo  $\text{W=O}$  of highly dispersed  $\text{WO}_x$  species [29,41]. This band shifted gradually from  $985 \text{ cm}^{-1}$  to  $970 \text{ cm}^{-1}$  with increasing  $\text{ZrO}_2$  content from 5 to 15% (trace c–e), reflecting the transformation from a polytungstate species gradually into an isolated monotungstate species [29,42–44]. The Raman results suggest that increasing the content of  $\text{ZrO}_2$  helps stabilize the highly dispersed  $\text{WO}_x$  surface species through forming Zr-stabilized  $\text{WO}_x$  clusters [27,45] and prevents the formation of large perfect crystallite  $\text{WO}_3$  particle on SBA-15, due to the strong interaction between tungsten and zirconium in the supported oxides.

Fig. 5 shows diffuse reflectance UV-vis spectra of  $\text{WZr/SBA-15}$  samples.  $\text{W}_{30}\text{Zr}_0/\text{SBA-15}$  exhibited a strong absorption band at  $\sim 389 \text{ nm}$ , accompanied by relatively weak bands at 218 and 273 nm (trace a). These bands are related to crystalline  $\text{WO}_3$  [46,47], isolated  $\text{WO}_4$  tetrahedral species [40,48,49], and partially polymerized W species in octahedral coordination [40,47], respectively. Since the absence of  $\text{ZrO}_2$  in this sample, the presence of the band at 218 nm suggests that besides the large crystalline  $\text{WO}_3$  on the external surface, a fraction of isolated W atoms are well dispersed in the framework of SBA-15. The strong band at 389 nm decreased

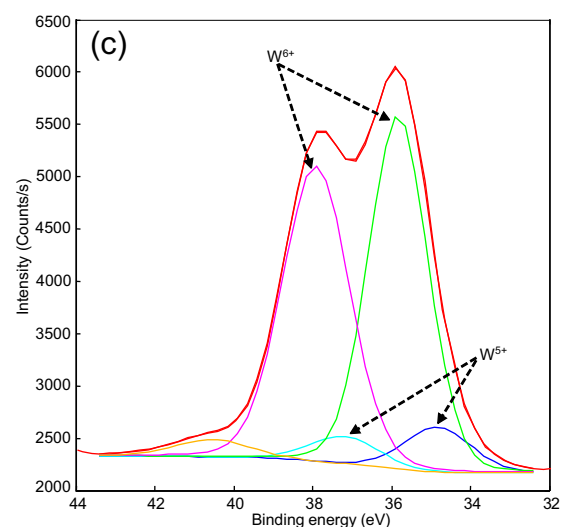
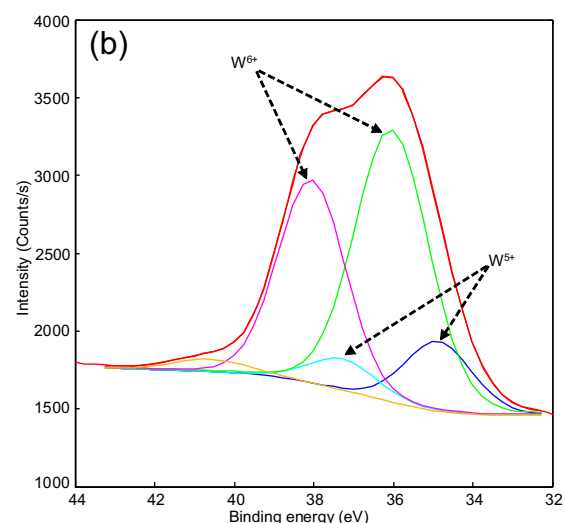
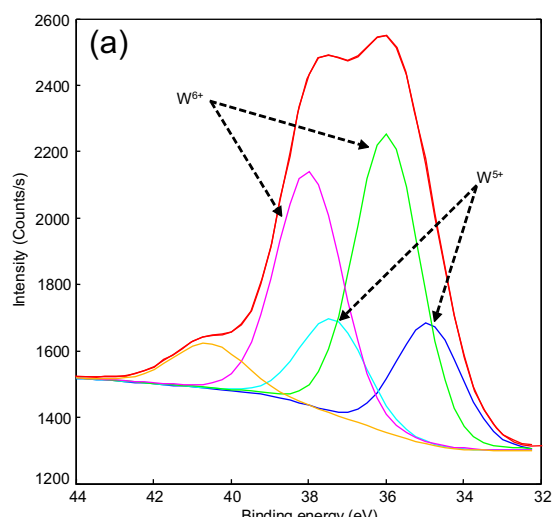


**Fig. 6.** X-ray photoelectron spectra of  $\text{W}_{4f}$  of (a)  $\text{W}_{30}\text{Zr}_0/\text{SBA-15}$ , (b)  $\text{W}_{30}\text{Zr}_5/\text{SBA-15}$ , (c)  $\text{W}_{30}\text{Zr}_{15}/\text{SBA-15}$  samples.

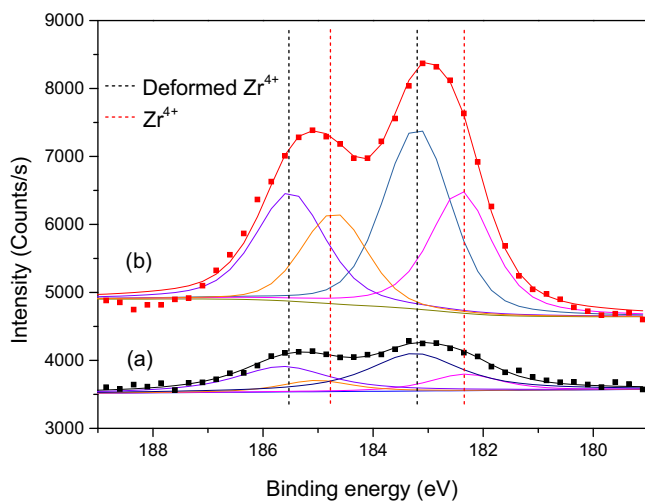


**Fig. 7.** X-ray photoelectron spectra of Zr<sub>3d</sub> of (a) W<sub>30</sub>Zr<sub>5</sub>/SBA-15, (b) W<sub>30</sub>Zr<sub>15</sub>/SBA-15 samples.

in intensities and disappeared when increasing amounts of ZrO<sub>2</sub> were doped (trace b and c), while the bands centered at around 273 nm and 218 nm became dominant. This result indicates that the stronger interaction of ZrO<sub>x</sub>-WO<sub>x</sub> over WO<sub>x</sub>-SiO<sub>2</sub> and WO<sub>x</sub>-WO<sub>x</sub> prevents the formations of isolated tungsten species in the framework and/or large WO<sub>3</sub> particles on the external surface of SBA-15, but helps the formation of polytungstate species and monotungstate species with the adjacent ZrO<sub>x</sub> species dispersed in the channel of SBA-15. Note that the bands intensities of 218 and 273 nm are slightly changed for the samples of W<sub>30</sub>Zr<sub>5</sub>/SBA-15 and W<sub>30</sub>Zr<sub>15</sub>/SBA-15 with increasing ZrO<sub>2</sub> loading. This might be a result of the distribution of monotungstate and polytungstate species changed from inside of the framework of SBA-15 to the surface to interact with zirconium species, as ZrO<sub>2</sub> content increasing. However, we can not rigorously differentiate the tungsten species interacting with SiO<sub>2</sub> in the framework of SBA-15 or with ZrO<sub>2</sub> on the surface in the UV-vis spectra at present.

The electronic environment and oxidation state of tungsten and zirconium species in the WZr/SBA-15 sample were investigated by XPS. Fig. 6 shows the XPS spectra of the W<sub>4f</sub> region. The peaks at binding energies of 35.7 eV and 37.8 eV can be assigned to the W<sup>6+</sup> species, while the peaks at 34.7 eV and 36.8 eV are associated with W<sup>5+</sup> species [32]. A small peak at ~41 eV in all samples is due to W<sub>5p3/2</sub>. An analysis of the results (Table 2) showed that the W<sup>5+)/(W<sup>5+</sup> + W<sup>6+</sup>) ratio reduced from 29% for W<sub>30</sub>Zr<sub>0</sub>/SBA-15 to 17% for W<sub>30</sub>Zr<sub>5</sub>/SBA-15, and further to 11% for W<sub>30</sub>Zr<sub>15</sub>/SBA-15. Clearly, the addition of ZrO<sub>2</sub> stabilized the W species in the more oxidized states through the strong Zr-W interactions. This strong interaction is further confirmed by the analysis of the Zr<sub>3d</sub> spectra. As shown in Fig. 7, curve fittings display two doublets at 182.3, 185.0 eV and 183.3, 185.5 eV, which are related to the Zr<sub>3d5/2</sub> and Zr<sub>3d3/2</sub> doublet of the Zr<sup>4+</sup> cations and strongly deformed Zr<sup>4+</sup> cations, respectively [26]. The strong interaction between the Zr-W deforms the electric field around the Zr<sup>4+</sup> nuclei due to the high electron attractor effect of the neighboring W atoms [26]. The ratio of Zr<sup>4+</sup> to deformed Zr<sup>4+</sup> increased with increasing ZrO<sub>2</sub> loading, which suggests the formation of clusters of ZrO<sub>2</sub> when excess ZrO<sub>2</sub> was loaded. The numerical results of XPS are summarized in Table 2. It is evident that the surface concentration of W increased as a function of the amount of doped Zr. The low W content in the sample of W<sub>30</sub>Zr<sub>0</sub>/SBA-15 in the absence of Zr suggests that the tungsten species is either in the form of isolated W atoms in the framework of SBA-15 or aggregated as large WO<sub>3</sub> particles on the external surface of SBA-15, consistent with the TEM, XRD, Raman, UV-vis results. The strongly preferred</sup>

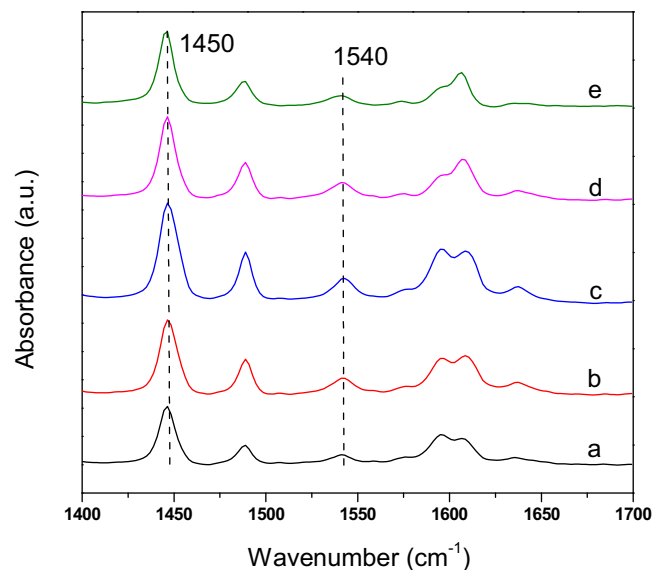


**Fig. 8.** FT-IR spectra of pyridine adsorption on (a) W<sub>30</sub>Zr<sub>0</sub>/SBA-15, (b) W<sub>30</sub>Zr<sub>3</sub>/SBA-15, (c) W<sub>30</sub>Zr<sub>5</sub>/SBA-15, (d) W<sub>30</sub>Zr<sub>10</sub>/SBA-15 and (e) W<sub>30</sub>Zr<sub>15</sub>/SBA-15.

interaction between Zr and W favors the formation of Zr-WO<sub>3</sub> tiny particles located inside the channel of SBA-15, but inhibits the interaction of W-Si and therefore the formation of isolated species in the framework of SBA-15, and prevents the formation of large aggregates of crystalline WO<sub>3</sub>. As the doped Zr was increased, more tungstate species was extracted to interact with Zr on the surface, resulting in increased concentration of surface tungsten species.

#### 4.3. Quantification of acid sites (FTIR of pyridine adsorption and NH<sub>3</sub>-TPD)

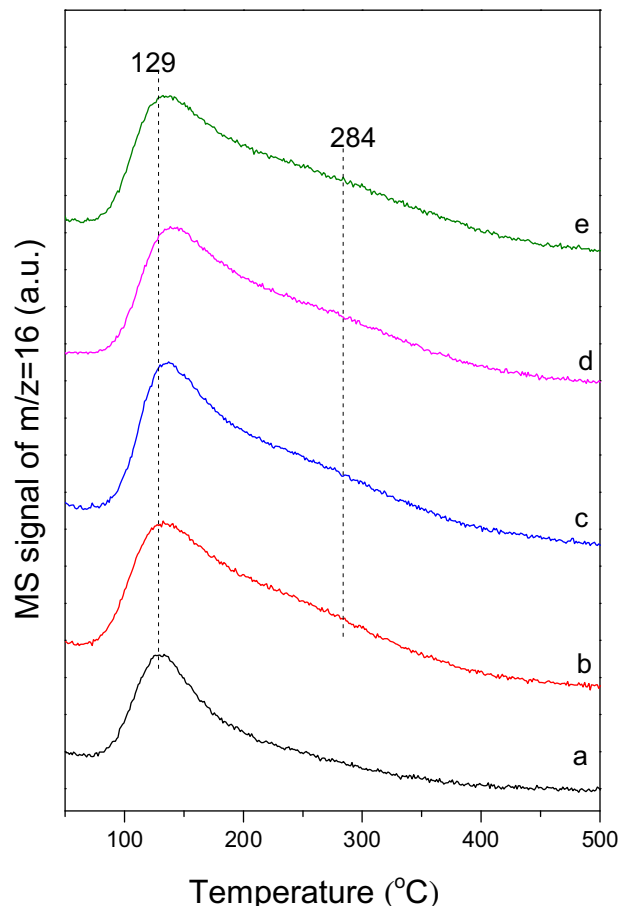
The infrared spectra of pyridine adsorption on WZr/SBA-15 catalysts are displayed in Fig. 8. The band at 1450 cm<sup>-1</sup> corresponds to the coordinated pyridine adsorption on the Lewis acid sites (LAS), and the band at 1540 cm<sup>-1</sup> is related to pyridine ions formed by interacting with Brønsted acid sites (BAS) [50]. All samples contain both BAS and LAS. Their peak intensities increased with increasing ZrO<sub>2</sub> content up to 5%, and then decreased if further increasing ZrO<sub>2</sub> content. The quantified acid densities are summarized in Table 1. The BAS density, total acid density and B/L ratio are maximized at a ZrO<sub>2</sub> content of 5%. The acid strength was studied by NH<sub>3</sub>-TPD. As shown in Fig. 9, only one low-temperature desorption peak at 129 °C is observed for the sample without of ZrO<sub>2</sub> (W<sub>30</sub>Zr<sub>0</sub>/SBA-15), which is characterized by weak acid strength. Besides this peak, a broad peak centered at ~284 °C with its tail extending to 400 °C is present for all samples with ZrO<sub>2</sub> doping, pointing to the presence of strong acid sites. The high-temperature desorption peak is of similar shape for all samples, which might indicate that the strong acid sites are of similar strength.

As revealed by XRD, Raman and UV-vis, the tungstate species over W<sub>30</sub>Zr<sub>0</sub>/SBA-15 are mainly bulk WO<sub>3</sub> crystallites, which are expected to be of low acidity due to the low exposure of the tungstate sites. The crystalline WO<sub>3</sub> shows mainly LAS property, which originates from the unsaturated W<sup>6+</sup> species. Even at the same amount of W loading, the Zr modified catalysts showed a much higher acid density than that of W<sub>30</sub>Zr<sub>0</sub>/SBA-15. Addition of ZrO<sub>2</sub> resulted in the formation of the surface polytungstate species due to the presence of a strong Zr and W interaction in the sample. The surface polytungstate species is maximized at 5% ZrO<sub>2</sub> loading. Consequently, the acid density increases as the ZrO<sub>2</sub> content is increased, up to 5%. According to the previous studies of

**Table 2**

The surface compositions of selected WZr/SBA-15 catalysts from XPS.

Catalyst	W <sup>5+</sup> /(W <sup>5+</sup> + W <sup>6+</sup> ) (%)	Zr <sup>4+</sup> /deformed Zr <sup>4+</sup>	Surface composition <sup>a</sup> (%)				Zr/W	W/Si
			O	Si	W	Zr		
W <sub>30</sub> Zr <sub>0</sub> /SBA-15	29	—	52.7	18.4	0.5	0	0	0.027
W <sub>30</sub> Zr <sub>5</sub> /SBA-15	17	0.35	47.6	18.2	1.0	0.4	0.4	0.055
W <sub>30</sub> Zr <sub>15</sub> /SBA-15	11	0.69	49.5	17.4	1.7	2.0	0.85	0.115

<sup>a</sup> C was not included.**Fig. 9.** The NH<sub>3</sub>-TPD profiles of WZr/SBA-15 samples (a) W<sub>30</sub>Zr<sub>0</sub>/SBA-15, (b) W<sub>30</sub>Zr<sub>3</sub>/SBA-15, (c) W<sub>30</sub>Zr<sub>5</sub>/SBA-15, (d) W<sub>30</sub>Zr<sub>10</sub>/SBA-15 and (e) W<sub>30</sub>Zr<sub>15</sub>/SBA-15.

the WO<sub>x</sub>/ZrO<sub>2</sub> catalysts [21,29], surface polytungstate species were suggested to be the sites with strong acidity of both Brønsted and Lewis types. Further increasing the ZrO<sub>2</sub> content led to the transformation of the polytungstate species to the isolated mono-tungstate species, which has a low acidity. In addition, the surface area was reduced in the samples with ZrO<sub>2</sub> loadings higher than 10% (Table 1), which may also reduce the amount of surface acid sites. Consequently, the measured acid density decreases.

#### 4.4. Catalytic performance of the WZr/SBA-15 catalysts for hydrolysis of cellobiose

##### 4.4.1. Catalytic activity

The catalytic activities of the WZr/SBA-15 catalysts in the hydrolyzing cellobiose are reported in Table 3. For comparison, a blank run in the absence of catalyst showed a low cellobiose conversion of 14.1%, with glucose yield of 9.6% (Entry 1). In the presence of WZr/SBA-15 catalysts, the conversion of cellobiose and the yield of monosaccharide increased significantly (Entry 2–6). As

seen in Table 3, the glucose and mannose are the major products, while glucopyranosyl-glucitol, erythrose, glycolaldehyde, levulinic acid, formic acid and 5-hydroxymethylfurfural are the minor ones. The conversion of cellobiose is 43.0%, with yields of glucose and mannose of 25.6% and 8.8%, respectively, over the W<sub>30</sub>Zr<sub>0</sub>/SBA-15 sample without ZrO<sub>2</sub>. All the WZr/SBA-15 catalysts containing ZrO<sub>2</sub> showed higher conversion of cellobiose and yield of monosaccharide than the W<sub>30</sub>Zr<sub>0</sub>/SBA-15 catalyst. The maximum conversion of cellobiose was achieved on the W<sub>30</sub>Zr<sub>5</sub>/SBA-15 catalyst, with a sugar yield of 52.6% (32.0% glucose and 20.6% mannose). However, the conversion of cellobiose and the yields of monosaccharide decreased gradually with the increasing ZrO<sub>2</sub> content beyond 5%.

To better understand the active phase of the catalyst in the conversion of cellobiose, the hydrolysis reaction was performed on several catalysts with different formulas. The results are listed in Table 3 (Entry 7–11). Either the physical mixture of ZrO<sub>2</sub>/SBA-15 + WO<sub>3</sub> or WO<sub>3</sub>/SBA-15 + ZrO<sub>2</sub> (Entry 8 and 9) showed significant lower activity than the W<sub>30</sub>Zr<sub>5</sub>/SBA-15 catalyst. This result highlights the crucial role of the strong interaction between Zr and W species in the WZr/SBA-15 catalyst prepared by hydrothermal one-step method played in the high activity of cellobiose hydrolysis. A reference sample of unsupported W<sub>30</sub>Zr<sub>5</sub> showed significantly lower conversion of cellobiose (Entry 11) than the W<sub>30</sub>Zr<sub>5</sub>/SBA-15 catalyst. Another reference catalyst of 30% WO<sub>3</sub>/ZrO<sub>2</sub> prepared by conventional impregnation method yielded a 39.5% conversion of cellobiose (Entry 7), which was far less than that on the W<sub>30</sub>Zr<sub>5</sub>/SBA-15 catalyst. These results indicate that the ordered mesoporous structure is essential to stabilize the highly dispersed surface Zr-WO<sub>x</sub> clusters to achieve high catalytic efficiency. Finally, a reference sample of 20% WO<sub>3</sub>/ZrO<sub>2</sub>, which showed optimized structure (maximum amounts of surface Zr-WO<sub>x</sub> clusters) to achieve the highest activity in methanol dehydration to dimethylether [27], was also tested for the hydrolysis of cellobiose. The resulting conversion is 44.8%, with yields of 17.3% glucose and 6.9% mannose (Entry 10). Again, the activity is significantly lower than that of the W<sub>30</sub>Zr<sub>5</sub>/SBA-15 sample. This further confirms that the mesoporous structure plays a significant role in the dispersion of the active species for hydrolysis.

##### 4.4.2. Correlating the structure and Brønsted acid density with the catalytic performance

Fig. 10 shows the conversion of cellobiose, specific surface area and BAS density as a function of ZrO<sub>2</sub> loading. All data showed a volcano-type dependence on ZrO<sub>2</sub> content. The cellobiose conversion, specific surface area and BAS density enhanced with the increase in the ZrO<sub>2</sub> loading up to 5%. After that, all of them decreased gradually. On one hand, the addition of the Zr species helps the dispersion of the W species and prevents the aggregation of the tungstate species into WO<sub>3</sub> crystalline. The dispersed Zr-WO<sub>3</sub> constitutes most of the acid sites. On the other hand, doping ZrO<sub>2</sub> stabilizes the mesoporous structure of SBA-15 and increased its specific surface area, which benefits the accessibility of the highly dispersed active sites by the bulky reactant like cellobiose. This correlation revealed that both catalyst structure and active acidic sites are essential to achieve a high activity for the hydrolysis of cellobiose.

**Table 3**

Comparison of conversion and major product yield during cellobiose hydrolysis over different catalysts.

Entry	Catalyst	Conversion (%)	Yield (%)								$\sum$ HPLC <sup>a</sup>
			Glu.	Man.	Glu-g.	Ery.	GA	LA	FA	5-HMF	
1	None	14.1	9.6	—	2.3	0	0.9	0	0	1.2	14.0
2	W <sub>30</sub> Zr <sub>0</sub> /SBA-15	43.0	25.6	8.8	4.6	0.7	2.2	0	0	0.3	42.2
3	W <sub>30</sub> Zr <sub>3</sub> /SBA-15	69.4	30.1	18.7	3.5	2.7	5.7	1.2	1.3	1.7	64.9
4	W <sub>30</sub> Zr <sub>5</sub> /SBA-15	75.0	32.0	20.6	3.8	2.7	7.1	1.3	1.4	1.6	70.5
5	W <sub>30</sub> Zr <sub>10</sub> /SBA-15	73.5	31.2	19.8	4.0	2.5	6.9	1.4	1.5	1.8	69.1
6	W <sub>30</sub> Zr <sub>15</sub> /SBA-15	60.9	27.4	14.6	3.5	1.9	4.5	1.6	1.7	2.1	57.3
7	30%WO <sub>3</sub> /ZrO <sub>2</sub>	39.5	19.0	7.4	4.4	0	0	1.4	1.6	2.8	36.6
8	7.1%ZrO <sub>2</sub> /SBA-15 (0.07 g)+WO <sub>3</sub> (0.03 g) <sup>b</sup>	29.4	20.4	4.3	2.1	0	0	0	0	0.7	27.5
9	31.6%WO <sub>3</sub> /SBA-15(0.095 g)+ZrO <sub>2</sub> (0.005 g) <sup>b</sup>	42.1	24.9	9.7	5.1	0.5	1.2	0	0	0	41.4
10	20%WO <sub>3</sub> /ZrO <sub>2</sub>	44.8	17.3	6.9	6.8	1.1	4.6	0.2	0.1	1.4	38.4
11	W <sub>30</sub> Zr <sub>5</sub>	34.1	12.5	4.0	7.0	1.2	1.3	0	0	0	26.0

Reaction conditions: cellobiose (0.2 g), catalysts (0.1 g), H<sub>2</sub>O (20 g), N<sub>2</sub> (2.5 MPa), T = 160 °C, reaction time is 90 min. Glu., Man., Glu-g., Ery., GA, LA, FA, 5-HMF stand for glucose, mannose, glucopyranosyl-glucitol, erythrose, glycolaldehyde, levulinic acid, formic acid and 5-hydroxymethylfurfural, respectively.

<sup>a</sup>  $\sum$  HPLC is the total yield of product which can be detected by high performance liquid chromatography.

<sup>b</sup> The resulting WO<sub>3</sub> loading and ZrO<sub>2</sub> loading were 30% and 5%, respectively, in the physical mixture.

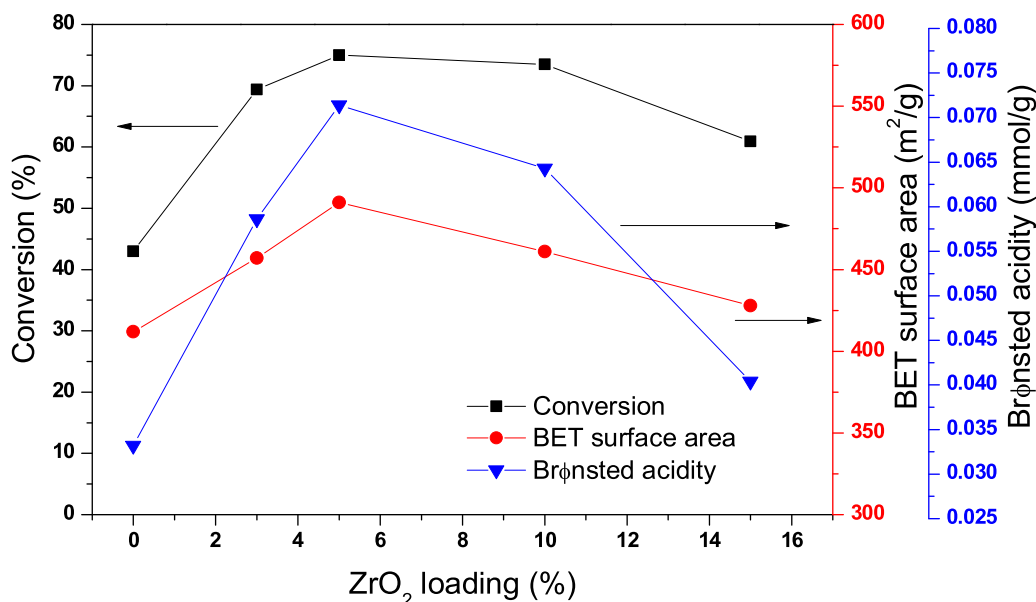


Fig. 10. Cellobiose conversion, BET surface area and Brønsted acid density as a function of ZrO<sub>2</sub> loading over W<sub>30</sub>Zr<sub>y</sub>/SBA-15(y = 0, 3, 5, 10, 15) catalysts.

It has been shown that the strong BAS catalyzes the hydrolysis of β-1,4-glycosidic bonds, and LAS promotes the hydrolysis by coordinately adsorption of reactant [51]. As indicated by the XRD and Raman results, a major fraction of the WO<sub>x</sub> species in W<sub>30</sub>Zr<sub>0</sub>/SBA-15 existed as large WO<sub>3</sub> crystalline, which is characterized by a low BAS density. Thereby, its catalytic activity is the lowest among the WZr/SBA-15 catalysts. Doping proper amount of ZrO<sub>2</sub> stabilizes the tiny WO<sub>3</sub> domains in the state of surface polytungstate. According to the studies on the WO<sub>x</sub>/ZrO<sub>2</sub> catalysts [21,52], the surface polytungstate species contributes to both the strong BAS and LAS, which provides the active sites for hydrolysis. In addition, the doped ZrO<sub>2</sub> increases the surface area, which makes the active sites accessible by the bulky reactant like cellobiose. As a result, doping ZrO<sub>2</sub> improved the activity of hydrolysis significantly, and the maximums of conversion and yield were achieved on W<sub>30</sub>Zr<sub>5</sub>/SBA-15. However, excessive ZrO<sub>2</sub> loading (>10%) transformed the polytungstate species to the isolated monotungstate species, which has low acid density. Moreover, excessive ZrO<sub>2</sub> also reduces the surface area, which is likely to hinder the accessibility of the active site by the bulky reactant. Therefore, the conversion and yield decreased when the ZrO<sub>2</sub> loading is higher than 5%. It should be noted that all strong acid sites have similar acid strength

in the ZrO<sub>2</sub> containing samples (NH<sub>3</sub>-TPD results). It can therefore be inferred that the differences in the hydrolysis activity of cellobiose over these WZr/SBA-15 catalysts are mainly dependent on the number of accessible strong acid sites.

#### 4.4.3. Effect of reaction time on the cellobiose hydrolysis over the W<sub>30</sub>Zr<sub>5</sub>/SBA-15 catalyst

Fig. 11 illustrates the conversion of cellobiose and the product distributions over the W<sub>30</sub>Zr<sub>5</sub>/SBA-15 catalyst as a function of reaction time. The conversion of cellobiose increased monotonically as the reaction time (Fig. 11a). Glucose and its isomer, mannose, are the major products (Scheme 1, cleavage A). Their yields increased gradually in the first 90 min, and then decreased when the reaction time was further prolonged (Fig. 11b), indicating that they converted to other products at a longer reaction time. In competition with the primary reaction of forming glucose from hydrolyzing the β-1,4-glycosidic bond between two glucose monomers, the hydrolysis of the C—O—C ether bond in a monomer results in the formation of glucopyranosyl-glucitol (Scheme 1, cleavage B) [53]. Its yield was 4% at 15 min, and decreased as the reaction time increases, which indicated that the glucopyranosyl-glucitol formed in the primary reaction could subject to further hydrolysis. It is interesting to note

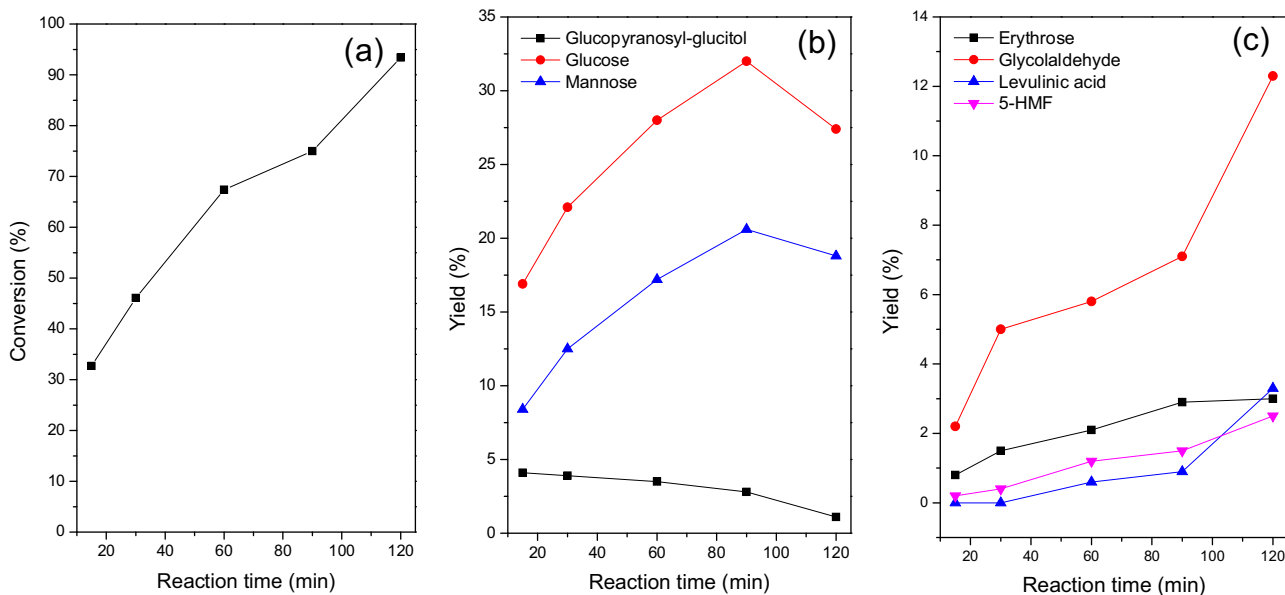


**Fig. 11.** Effect of reaction time on (a) cellobiose conversion, (b) major product and (c) minor product distributions on the  $\text{W}_{30}\text{Zr}_5/\text{SBA-15}$  catalyst. Reaction conditions: cellobiose (0.2 g), catalysts (0.1 g),  $\text{H}_2\text{O}$  (20 g),  $\text{N}_2$  (2.5 MPa),  $T = 160^\circ\text{C}$ .

that the mannose yield on these tungstate rich catalysts is significantly higher than those on the Brønsted acid type catalysts, but is similar to those on the supported molybdate catalysts [54,55]. It has been reported that molybdate dimer could adsorb glucose through interaction with the hydroxyl groups connecting to C1–C4 carbon atoms and facilitate the forming C1–C3 bond at the expense of breaking the C2–C3 bond, leading to the formation of mannose [56]. Since Mo and W are the elements of the same group, one may expect that the tungstate dimmers formed on the Zr stabilized  $\text{WO}_3$  tiny clusters on  $\text{WZr}/\text{SBA-15}$  catalysts are able to catalyze the isomerization of glucose to mannose in a similar way as that has been proposed on the molybdate catalyst.

The yields of the minor products (glycolaldehyde (from 7.1% to 12.3%), levulinic acid (from 0.9% to 3.3%), 5-hydroxymethylfurfural (5-HMF, from 1.5% to 2.5%) increase with the increasing reaction time (Fig. 11c). As shown in Scheme 1, the primarily formed monosaccharide dissociated into erythrose and glycolaldehyde by retro aldol reaction on LAS, and erythrose was further dissociated into glycolaldehyde [57]. In the meantime, monosaccharide can also dehydrate into 5-hydroxymethylfurfural on BAS, which could further convert into levulinic acid [58]. This experiment indicates that the maximum yields of primary products of monosaccharides are achieved at reaction time of 90 min before they further converts significantly to the secondary products. It is worth noting that notable fructose was not detected in current work. Even though it is generally accepted that fructose is more facile to be dehydrated to 5-HMF, it has been reported that the glucose can be directly dehydrated to 5-HMF [59]. It seems that in our work, the  $\text{WO}_3$  rich catalyst is more active for glucose to isomerize to mannose over to fructose. In addition, this catalyst seems little active for direct dehydration of glucose to 5-HMF. Indeed, very low yield of 5-HMF was observed over all catalysts (Table 3 and Fig. 11). The low yield to 5-HMF lowers the chance for its condensation with glucose and its self condensation for the formation of humins [58–60]. As a result, the observed carbon balance (see Table 3) is relatively high under current reaction conditions.

#### 4.4.4. Recycling of $\text{W}_{30}\text{Zr}_5/\text{SBA-15}$ catalyst

In order to evaluate the reusability of the most promising catalyst identified in this work,  $\text{W}_{30}\text{Zr}_5/\text{SBA-15}$  was tested in sev-

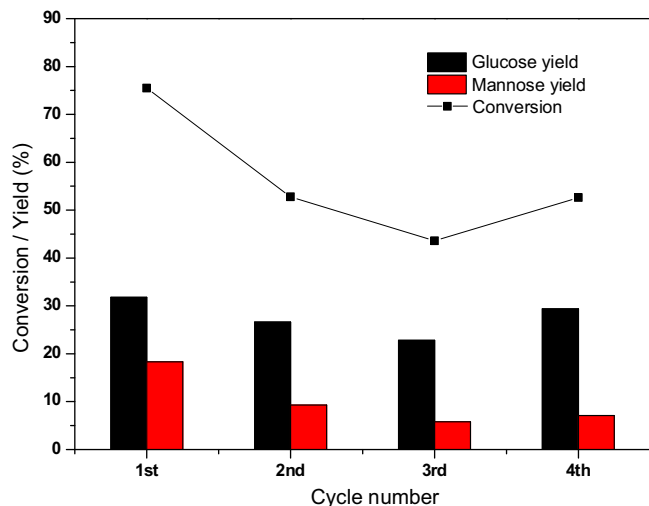
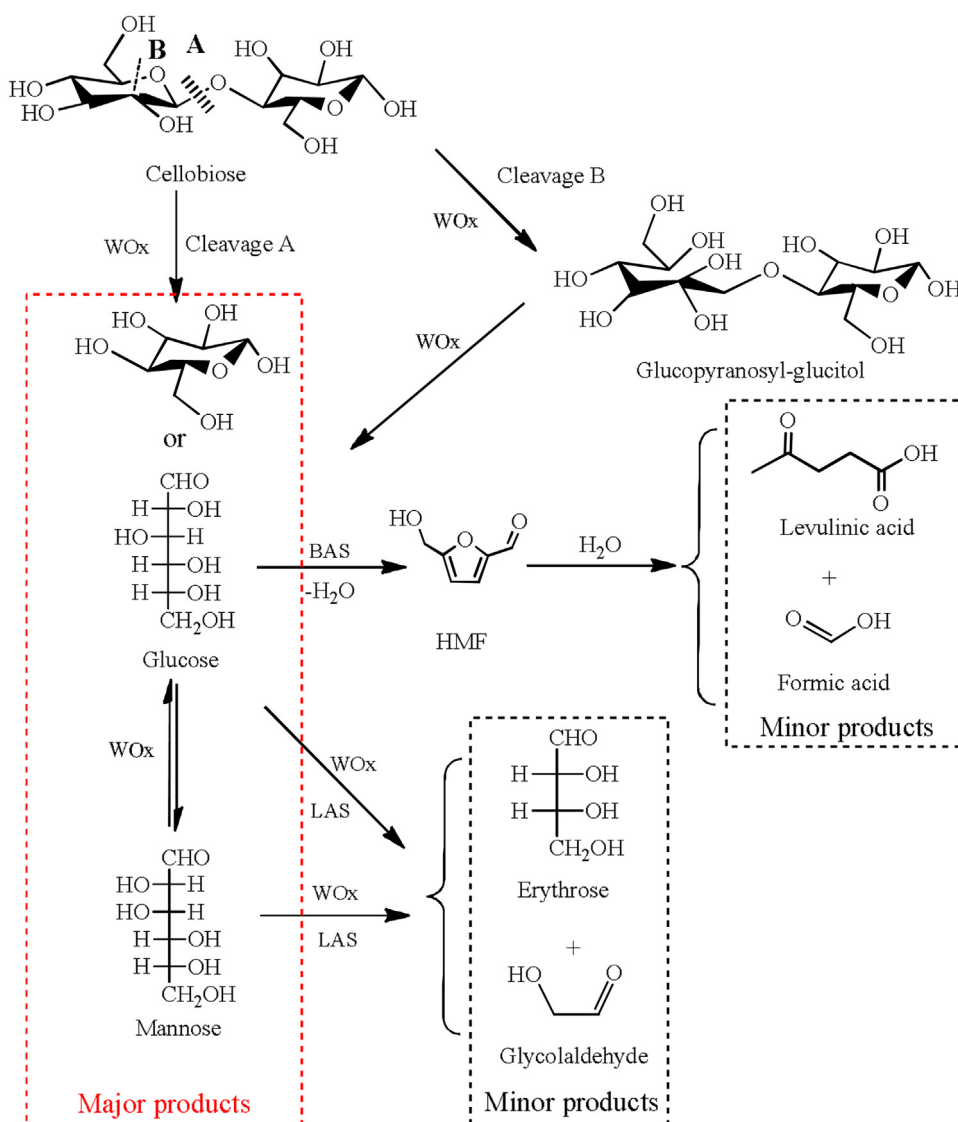


**Fig. 12.** Reusability of the  $\text{W}_{30}\text{Zr}_5/\text{SBA-15}$  catalyst for cellobiose hydrolysis. Reaction conditions:  $\text{N}_2$  (2.5 MPa),  $T = 160^\circ\text{C}$ , reaction time is 90 min. The amount of cellobiose and  $\text{H}_2\text{O}$  was scaled according to the recovered amount of catalyst (cellobiose<sub>initial</sub> (0.3 g), catalysts<sub>initial</sub> (0.15 g),  $\text{H}_2\text{O}$ <sub>initial</sub> (30 g)). The recovered catalyst was washed by water and ethanol for five cycles, then dried overnight in the oven at 353 K.

eral consecutive catalytic cycles. After each run, the catalyst was washed with ethanol and water at room temperature followed by filtration and drying at  $80^\circ\text{C}$ . The results are shown in Fig. 12. Compared with the first run, both the conversion of cellobiose and the yield of glucose and mannose decreased drastically in the second run. The decrease slowed down in the subsequent runs. Inductively coupled plasma (ICP) analysis of the used catalysts shows that leaching of W was significant at the first run (35%), while it was slow in the subsequent runs with 52% W loss after the fourth run. This result indicates that most of the W species with weak interactions with  $\text{ZrO}_2$  was leached at the first run, and the remaining W species with strong interaction with  $\text{ZrO}_2$  was leached slowly in the subsequent runs.



**Scheme 1.** The pathway of cellobiose conversion over WZr/SBA-15 catalysts.

## 5. Conclusions

High surface area WZr/SBA-15 catalysts ( $>400\text{ m}^2/\text{g}$ ) were prepared and characterized. XRD and  $\text{N}_2$  adsorption results showed that doping  $\text{ZrO}_2$  into the  $\text{W}_{30}\text{Zr}_y/\text{SBA-15}$  catalyst preserved the SBA-15 structure with improved surface areas. Characterization with TEM and XRD showed that the strong Zr-W interaction in the  $\text{W}_{30}\text{Zr}_y/\text{SBA-15}$  catalyst prevented the aggregation of  $\text{WO}_3$  into large crystallite. Raman, UV-vis and XPS results further support the existence of the strong interaction between the zirconium and tungstate species, which helps the dispersion of the W species, preventing the aggregation of the tungstate species into  $\text{WO}_3$  crystalline. This strong interaction also provides strong Brønsted acid sites with improved acid density and accessibility to the bulky reactant. The improvement was maximized at the  $\text{ZrO}_2$  loading of 5%. Excessive  $\text{ZrO}_2$  beyond 5% results in a transformation of the surface polytungstate species into the isolated monotungstate species as well as extraction of the tungstate species from the framework to the external surface, resulting in reduced surface area and acid density.

The measured activity for cellobiose hydrolysis correlates with the structure of the catalysts. A  $\text{ZrO}_2$  loading of 5% resulted in max-

imized the surface area and Brønsted acid density, thereby, the highest catalytic activity toward cellobiose hydrolysis. And this catalytic activity is much higher than that achieved on the  $\text{WO}_3/\text{ZrO}_2$  catalyst prepared using the conventional impregnation method. This result indicates that the density of the strong Brønsted acid site with improved accessibility by the bulky reactant of cellobiose is essential to achieve a high activity for biomass hydrolysis.

## Acknowledgments

The work was supported by Natural Science Foundation of China (Grant No. 21076152 and No. 21276191).

## Appendix A. Supplementary data

Supplementary data associated with this article can be found, in the online version, at <http://dx.doi.org/10.1016/j.apcata.2016.06.006>.

## References

- [1] A.M. Ruppert, K. Weinberg, R. Palkovits, *Angew. Chem.* **51** (2012) 2564–2601.

- [2] D.M. Alonso, S.G. Wettstein, J.A. Dumesic, *Chem. Soc. Rev.* 41 (2012) 8075–8098.
- [3] H. Kobayashi, H. Ohta, A. Fukuoka, *Catal. Sci. Technol.* 2 (2012) 869–883.
- [4] M. Yabushita, H. Kobayashi, A. Fukuoka, *Appl. Catal. B: Environ.* 145 (2014) 1–9.
- [5] K. Fabičovcová, O. Malter, M. Lucas, P. Claus, *Green Chem.* 16 (2014) 3580–3588.
- [6] W.P. Deng, Q.H. Zhang, Y. Wang, *Catal. Today* 234 (2014) 31–41.
- [7] J.X. Xi, D.Q. Ding, Y. Shao, X.H. Liu, G.Z. Lu, Y.Q. Wang, *ACS Sustain. Chem. Eng.* 2 (2014) 2355–2362.
- [8] X.N. Xie, J.Y. Han, H. Wang, X.L. Zhu, X. Liu, Y.F. Niu, Z.Q. Song, Q.F. Ge, *Catal. Today* 233 (2014) 70–76.
- [9] H. Wang, J. Lv, X.L. Zhu, X. Liu, J.Y. Han, Q.F. Ge, *Top. Catal.* 58 (2015) 623–632.
- [10] H. Kobayashi, A. Fukuoka, *Green Chem.* 15 (2013) 1740–1763.
- [11] Y.B. Huang, Y. Fu, *Green Chem.* 15 (2013) 1095–1111.
- [12] N. Rajabbeigi, A.I. Torres, C.M. Lew, B. Elyassi, L.M. Ren, Z.P. Wang, H. Je Cho, W. Fan, P. Daoutidis, M. Tsapatsis, *Chem. Eng. Sci.* 116 (2014) 235–242.
- [13] G. Gliozzi, A. Innorta, A. Mancini, R. Bortolo, C. Perego, M. Ricci, F. Cavani, *Appl. Catal. B: Environ.* 145 (2014) 24–33.
- [14] A. Charmot, P.W. Chung, A. Katz, *ACS Sustain. Chem. Eng.* 2 (2014) 2866–2872.
- [15] L.P. Zhou, Z. Liu, M.T. Shi, S.S. Du, Y.L. Su, X.M. Yang, J. Xu, *Carbohydr. Polym.* 98 (2013) 146–151.
- [16] F. Schüth, R. Rinaldi, N. Meine, M. Käldström, J. Hilgert, M.D. Kaufman Rechulski, *Catal. Today* 234 (2014) 24–30.
- [17] Q.H. Zhang, M. Benoit, K. De Oliveira Vigier, J. Barrault, G. Jégou, M. Philippe, F. Jérôme, *Green Chem.* 15 (2013) 963–969.
- [18] J. Hilgert, N. Meine, R. Rinaldi, F. Schüth, *Energy Environ. Sci.* 6 (2013) 92–96.
- [19] F. Zhang, Z. Fang, *Bioresour. Technol.* 124 (2012) 440–445.
- [20] M.R. Liu, H. Wang, J.Y. Han, Y.F. Niu, *Carbohydr. Polym.* 89 (2012) 607–612.
- [21] R. Kourieh, S. Bennici, M. Marzo, A. Gervasini, A. Auoux, *Catal. Commun.* 19 (2012) 119–126.
- [22] F. Chambon, F. Rataboul, C. Pinel, A. Cabiac, E. Guillou, N. Essayem, *Appl. Catal. A: Gen.* 504 (2015) 664–671.
- [23] D.G. Barton, S.L. Soled, G.D. Meitzner, G.A. Fuentes, E. Iglesia, *J. Catal.* 181 (1999) 57–72.
- [24] J. Macht, C.D. Baertsch, M. May-Lozano, S.L. Soled, Y. Wang, E. Iglesia, *J. Catal.* 227 (2004) 479–491.
- [25] I.E. Wachs, T. Kim, E.I. Ross, *Catal. Today* 116 (2006) 162–168.
- [26] M.A. Cortés-Jácome, C. Angeles-Chavez, E. López-Salinas, J. Navarrete, P. Toribio, J.A. Toledo, *Appl. Catal. A: Gen.* 318 (2007) 178–189.
- [27] E.I. Ross-Medgaarden, W.V. Knowles, T. Kim, M.S. Wong, W. Zhou, C.J. Kiely, I.E. Wachs, *J. Catal.* 256 (2008) 108–125.
- [28] N. Soulitanidis, W. Zhou, A.C. Psarras, A.J. Gonzalez, E.F. Iliopoulos, C.J. Kiely, I.E. Wachs, M.S. Wong, *J. Am. Chem. Soc.* 132 (2010) 13462–13471.
- [29] K.S. Song, H.B. Zhang, Y.H. Zhang, Y. Tang, K.J. Tang, *J. Catal.* 299 (2013) 119–128.
- [30] T. Li, S.T. Wong, M.C. Chao, H.P. Lin, C.Y. Mou, S. Cheng, *Appl. Catal. A: Gen.* 261 (2004) 211–219.
- [31] I. Jiménez-Morales, J. Santamaría-González, P. Maireles-Torres, A. Jiménez-López, *Appl. Catal. A: Gen.* 379 (2010) 61–68.
- [32] T.Y. Kim, D.S. Park, Y. Choi, J. Baek, J.R. Park, J. Yi, *J. Mater. Chem.* 22 (2012) 10021–10028.
- [33] C.A. Emeis, *J. Catal.* 141 (1993) 347–354.
- [34] X.L. Zhu, L.L. Lobban, R.G. Mallinson, D.E. Resasco, *J. Catal.* 271 (2010) 88–98.
- [35] Q.Q. Sun, G.Y. Chen, H. Wang, X. Liu, J.Y. Han, Q.F. Ge, X.L. Zhu, *ChemCatChem* 8 (2016) 551–561.
- [36] A. Bordoloi, S.B. Halligudi, *J. Catal.* 257 (2008) 283–290.
- [37] A. Bordoloi, A. Vinu, S.B. Halligudi, *Chem. Commun.* (2007) 4806–4808.
- [38] L.H. Hu, S.F. Ji, Z. Jiang, H.L. Song, P.Y. Wu, Q.Q. Liu, *J. Phys. Chem. C* 111 (2007) 15173–15184.
- [39] Y.Q. Zhang, S.J. Wang, J.W. Wang, L.L. Lou, C. Zhang, S.X. Liu, *Solid State Sci.* 11 (2009) 1412–1418.
- [40] E.I. Ross-Medgaarden, I.E. Wachs, *J. Phys. Chem. C* 111 (2007) 15089–15099.
- [41] M.N. Taylor, W. Zhou, T. Garcia, B. Solsona, A.F. Carley, C.J. Kiely, S.H. Taylor, *J. Catal.* 285 (2012) 103–114.
- [42] S.H. Zhu, X.Q. Gao, Y.L. Zhu, J.L. Cui, H.Y. Zheng, Y.W. Li, *Appl. Catal. B: Environ.* 158–159 (2014) 391–399.
- [43] T. Kim, A. Burrows, C.J. Kiely, I.E. Wachs, *J. Catal.* 246 (2007) 370–381.
- [44] D.E. Lopez, K. Suwannakarn, D.A. Bruce, J.G. Goodwinjr, *J. Catal.* 247 (2007) 43–50.
- [45] W. Zhou, E.I. Ross-Medgaarden, W.V. Knowles, M.S. Wong, I.E. Wachs, C.J. Kiely, *Nat. Chem.* 1 (2009) 722–728.
- [46] R. Maheswari, M.P. Pachamuthu, A. Ramanathan, B. Subramaniam, *Ind. Eng. Chem. Res.* 53 (2014) 18833–18839.
- [47] A. Ramanathan, R. Maheswari, B.P. Grady, D.S. Moore, D.H. Barich, B. Subramaniam, *Microporous Mesoporous Mater.* 175 (2013) 43–49.
- [48] D.R. Hua, S.L. Chen, G.M. Yuan, Y.L. Wang, *J. Porous Mater.* 18 (2011) 729–734.
- [49] A. Ramanathan, B. Subramaniam, D. Badloe, U. Hanefeld, R. Maheswari, *J. Porous Mater.* 19 (2012) 961–968.
- [50] L.F. Gong, Y. Lu, Y.J. Ding, R.H. Lin, J.W. Li, W.D. Dong, T. Wang, W.M. Chen, *Appl. Catal. A: Gen.* 390 (2010) 119–126.
- [51] K. Shimizu, H. Furukawa, N. Kobayashi, Y. Itaya, A. Satsuma, *Green Chem.* 11 (2009) 1627–1632.
- [52] J.R. Park, B.K. Kwak, D.S. Park, T.Y. Kim, Y.S. Yun, J. Yi, *Korean J. Chem. Eng.* 29 (2012) 1695–1699.
- [53] W. Deng, R. Lobo, W. Setthapun, S.T. Christensen, J.W. Elam, C.L. Marshall, *Catal. Lett.* 141 (2011) 498–506.
- [54] M.L. Hayes, N.J. Pennings, A.S. Serianni, R. Barker, *Am. Chem. Soc.* 104 (1982) 6764–6769.
- [55] Z. Hricovíničová-Bilíková, M. Hricovínič, M. Petrus'ová, A.S. Serianni, L. Petrus', *Carbohydr. Res.* 319 (1999) 38–46.
- [56] A. Köckritz, M. Kant, M. Walter, A. Martin, *Appl. Catal. A: Gen.* 334 (2008) 112–118.
- [57] F.D. Clipper, M. Dusselier, R.V. Rompaey, P. Vanelder, J. Dijkmans, E. Makshina, L. Giebel, S. Oswald, G.V. Baron, J.F.M. Denayer, P.P. Pescarmona, P.A. Jacobs, B.F. Sels, *J. Am. Chem. Soc.* 134 (2012) 10089–10101.
- [58] X. Hu, C.Z. Li, *Green Chem.* 13 (2011) 1676–1679.
- [59] S.J. Dee, A.T. Bell, *ChemSusChem* 4 (2011) 1166–1173.
- [60] A. Chuntanapum, Y. Matsumura, *Ind. Eng. Chem. Res.* 49 (2010) 4055–4062.